Dynamics of coreless defects during winding up transitions in confined chiral nematic liquid crystals

E. K. Omori
Departamento de Física, Universidade Estadual de Maringá, Avenida Colombo, 87020-900 Maringá, Brazil

R. F. de Souza
Senai Cimatec - Supercomputing Center for Industrial Innovation from Bahia State, Avenida Orlando Gomes 2845, CEP 41650-010 Salvador, Brazil

A. Jakli
Materials Sciences Graduate Program and Advanced Materials and Liquid Crystal Institute, Kent State University, Kent, Ohio 44242, USA

R. T. de Souza and R. S. Zola
Departamento de Física, Universidade Estadual de Maringá, Avenida Colombo, 87020-900 Maringá, Brazil and Departamento Acadêmico de Física, Universidade Tecnológica Federal do Paraná, Campus Apucarana, Rua Marcílio Dias, 635 86812-460 Apucarana, Brazil

(Received 9 August 2022; accepted 23 November 2022; published 20 December 2022)

Twist-coupled elastic deformations are ubiquitous and in the limelight of interest for next-generation self-shaping materials. Here, we describe how twist dynamics under fixed anchoring lead to bend deformation and defect dynamics in a field-unwound chiral liquid crystal material. We use the Q-tensor dynamics under the Landau–de Gennes formalism in a finite-element mesh to explore the texture pathways from the unwound (homeotropic) to the helical planar structure. Our simulations describe well previously reported experiments and confirm that the process occurs by forming pairs of coreless defects that interact with each other and create quadrupolar structures called Lehmann clusters. The dynamics and coarsening of dipoles and quadrupoles of defects are described. This numerical study describes the full dynamics, which has been sought for several years.

DOI: 10.1103/PhysRevE.106.064701

I. INTRODUCTION

The need to understand strained structures and self-shaping occurrence is ubiquitous in several fields of research and applications [1]. Spontaneous deformations, such as buckling, twisting, and wrinkling, are often credited to the need to release stored potential energy, which may exist due to external forces and confinement, for example. These deformations have potential applications such as in sensors, actuators, active matter, drug delivery, and many others [1,2]. One kind of material that often permeates as a candidate for achieving such applications is liquid crystal (LC), owing to the coupling between long-range order and responsiveness to external stimuli [3–8]. Elastic deformations may present coupled modes in LCs, depending on molecular shape [9], which represents potential use for shape-changing objects and may occur by the interplay of symmetry breaking such as chirality and confinement [10]. Nonetheless, understanding the dynamics of how such deformations come to be, rather than their static aspects, is crucial when designing new materials for state-of-the-art applications. This work focuses on the dynamic transition from unwound to twisted in confined cholesteric LCs (CLCs). CLCs are locally nematics but repeat themselves within a length called the pitch p, thus forming a helical shape in space. This transition, often referred to as the homeotropic-to-planar (H-to-P) transition [11], occurs during the relaxation process from the unwound to the wound-up state, and it has been studied, both theoretically and experimentally, in the past [12–20]. This transition is often studied by applying an external field to unwind the CLC helix in a confined sample, and then suddenly removing the field, so the confined helix can form. During this complex dynamics, director twists and buckling of layers take place. Yang and Lu first derived the elastic equations for the process [21], showing that, in the initial moments, the pitch is considerably larger than the natural value, more specifically, K_{33}/K_{22} times larger, where K_{33} and K_{22} are the bend and twist elastic constants, respectively. Usually, $K_{33} \approx 2K_{22}$, so this transient pitch is roughly twice the natural pitch. Later, several studies were dedicated to understanding the underlying mechanism from the unwound state, passing through the transient planar state until the final twisted state, either experimentally or employing computer simulations [13–20,22]. Accordingly, once the transient pitch is reached, the system evolution occurs by bending, followed by buckling of the layers. Following this step, most studies only propose possible routes for reaching the stable state since computer simulations often get trapped in metastable states. Still, experimentally a slow relaxation process toward homogeneity [22] occurs.

Some works discuss whether defects are formed in this process [14] or call it the focal-conic state [17]. Recently, Yu *et al.* [23] mixed calamitic with bent-dimer materials to change the ratio K_{33}/K_{22} from nearly 2 to less than 1. However, many of the details about the transition are still missing.

In this paper, we revisit the problem of the H-to-P transition utilizing modern computer simulations and analysis tools to unravel the dynamics of the transition. We study these dynamics for the case of strong (but finite) anchoring energy and compare this case with the free-surface case. The parameters indicating the local deformations [24] (S_{SB} and S_{TW}; see Supplemental Material (SM) [25]) are given during the process. Employing the proposed analysis, the entire dynamics can be described, including the movements of coreless defects.

II. METHODOLOGY

Our model solves the dynamical equation of nematodynamics without flow for a CLC sample. The dynamical evolution for the Q tensor is given in the Landau–de Gennes (LdG) formalism [26], described in the SM. The sample is a slab of dimensions $4.5 \times 4.5 \times 1.5$ μm, and we assume that the interaction of the CLC with the limiting substrates in the z direction is given in the Rapini-Papoular formalism. Periodic boundary conditions are assumed in the x and y directions. The CLC sample has $N = 12$ (number of π turns) and is initially in a perfect Grandjean state [11]. We then apply a strong electric field for 1 ms in the z direction, unwinding the helix. The field is then rapidly removed, and the material is allowed to rewind. The equations were discretized in the finite-element formalism and implemented in the COMSOL MULTIPHYSICS software. The time evolution is controlled by a variable-order backward difference formula (BDF). We set the elastic constant's value in the LdG formalism in terms of the Frank elastic constants by following the parametrization in Eq. (S3) [27], which is given in the SM. We used the ratios $K_{11}/K_{22} = 1.84$ and $K_{33}/K_{22} = 2.0$. We ran the dynamics for strong-anchoring and free-boundary cells, and we calculate the amount of splay, twist, and bend deformations and the total elastic energy in terms of the Frank free energy (see Fig. 9 below). We used several parameters to monitor the evolution of the twisted state, including the the S_{SB} parameter [24], the S_{TW} parameter [24], and the parameter Π [28]. Finally, we calculated the transient textures with the Mueller matrix method [11] and monochromatic and polychromatic light beam approximation. Further details are provided in the SM.

For the thermal parameters, we used $A = a(T - T^*) = -172 \times 10^9$ J/m^3, $B = -2.12 \times 10^6$ J/m^3, and $C = 1.73 \times 10^6$ J/m^3, all of which resulting in $S = 0.53$. To assure the ratio $K_{33}/K_{22} = 2$, the simulation was performed by using a set of elastic parameters similar to the MLC6608 host, that is, $K_{11} = 16.7$ pN, $K_{22} = 9.05$ pN, and $K_{33} = 18.1$ pN, which were converted into the L_i parameters through Eq. (S3) of the SM. Furthermore, we used $L_s = 0.0$ pN and $q_0 = 2.51 \times 10^7$ m^{-1}.

The interaction between the LC and the surfaces was evaluated utilizing Rapini-Papoular-like anchoring energy, given by Eq. (S4) of the SM, with an anchoring strength of 0.01 J/m^2, which represents a strong-anchoring situation [11]. Both simulated surfaces were constructed with the easy axis in the x direction with a pretilt of 1°; that is, the easy axis can be described by $\vec{n^0} = \cos 1^\circ \hat{i} + \sin 1^\circ \hat{k}$. The use of pretilt can prevent the formation of surface defects, but in the chiral case the pretilt also creates a preference of the system to have an even or odd number of twists.

A constant approximation was performed to simulate the electric field since the purpose was to enforce a homeotropic state in the system, at which the electric field would be approximately constant. To ensure the homeotropic state, a strong electric field, $E = 8.14 \times 10^7$ V m^{-1} $\hat{k}$, was applied for 1 ms. This field is four times higher, compared with the critical electric field, than either the planar-to-homeotropic or the fingerprint-to-homeotropic transition for a material with the above-mentioned elastic parameters and dielectric anisotropy of $\Delta_\epsilon = 4.2$. The mesh of these simulations was composed of tetrahedral elements, with a maximum edge length of 36 nm, using linear interpolation.

III. RESULTS

From the unwound state, the field is turned off ($t = 0$), and one first observes the formation of CLC layers arising from both surfaces and growing toward the center of the cell [Fig. 1(a)]. When $t = 1.37$ ms [Fig. 1(b)], the system has nearly completely formed the transient planar phase [11,22], with the pitch $p_{tp} = 2p_0$. The directors are fixed at the substrates, so the system is in a high-twist-energy state. To reduce the elastic stress, the system wrinkles by locally "bending" the CLC layers [22], which happens so further winding can occur, as shown in Fig. 1(c) for $t = 23.1$ ms. These deformations resemble Helfrich undulations [11] [see SM, Fig. S1(a-i)]; however, they are not homogeneous in the field of view [Fig. 1(d)], and so they do not form a square lattice. Rather, they are nonsymmetric deformations (see SM, Fig. S1). Figure 1(e) shows the evolution of the azimuthal angle across the cell.

As the wrinkle process continues, nonsingular defects [29] (λ lines) form in the regions of high-bend deformations [30], seen in Fig. 2(a). These λ lines are formed in $\lambda^{+1/2}$ and $\lambda^{-1/2}$ pairs (see also Fig. S2 of the SM), and their dynamics dictate how the material relaxes to the Grandjean state. At the apex of deformation, a pair of lines nucleate in the high-deformation zones and quickly displace the surrounding layers. This initial pair forms a structure with a total Burger vector b equal to the pitch ($b = p$) [31]. Notice that the tilted layers form a configuration similar to what is observed in developing parabolic walls [32], except that they occur near the center of the cell to balance chirality, elasticity, and surface energy. The pair of lines occurs everywhere in the field of view and near the center of the cell (in the z direction), with one line on top and the other line completing the pair, a few planes below. We shall name pairs where the $+1/2$ line is on top a "positive pair," or p pair, and the ones where the $-1/2$ line is on top a "negative pair," or n pair. From the initial deformation, p pairs and n pairs form almost simultaneously and near each other, although at different slip planes compared with the substrates (see SM, Fig. S3). The formed lines are nearly 700 nm in length and nearly 100 nm wide. After n pairs and p pairs appear, the fingerprint (FP) texture is fully

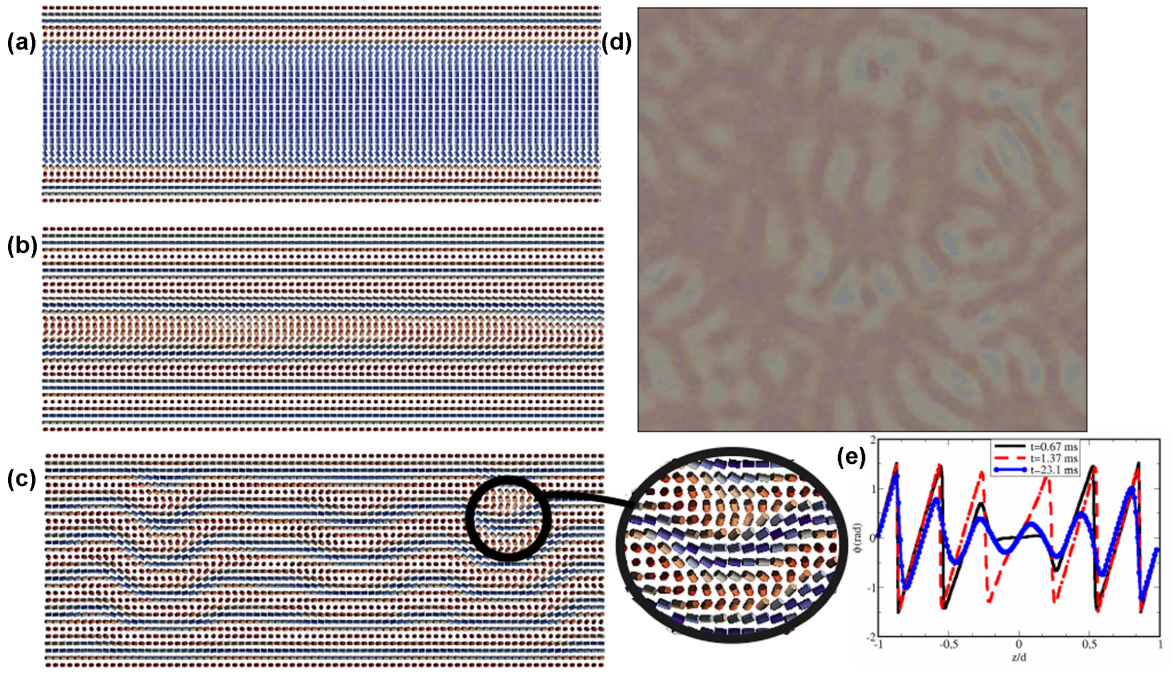

FIG. 1. (a)–(c) show the director field across the sample (top to bottom is the z direction, and right to left is the x direction), where the blue colors indicate in-plane orientation while the red colors indicate out-of-plane orientation. The sample starts winding up from the surfaces (a), passing through the transient planar structure (b) until undulations (c) arise as a way of decreasing the pitch toward the natural pitch. (d) shows the calculated optical texture. (e) shows the azimuthal angle across the sample for three different times. The solid black line is for $t = 0.67$ ms, the dashed orange line is for $t = 1.37$ ms, and the solid blue line is for $t = 23.1$ ms.

formed, and the pairs of lines correspond to the center of a double spiral structure often seen in the FP texture. The pairs of lines correspond to the central region of a large domain of displaced layers that wrap the pairs of lines. This is seen in Fig. 2(b), where the calculated fingerprint texture is shown

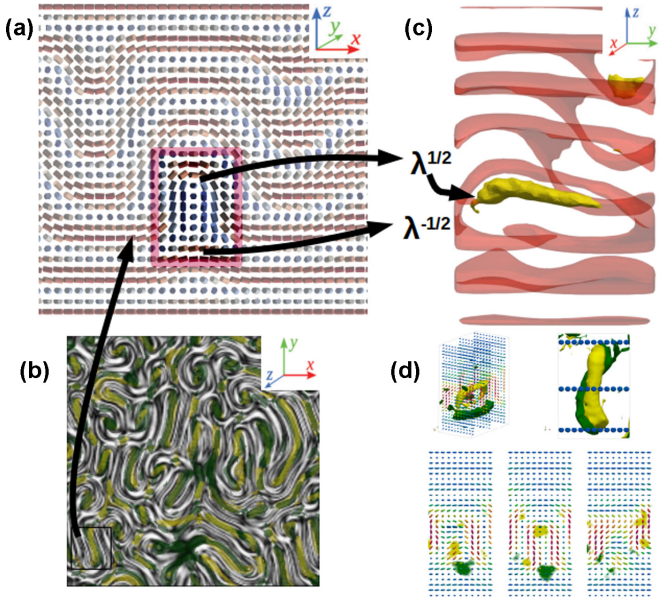

FIG. 2. Nucleation of pairs of λ lines in highly deformed regions (a). The lines displace the surrounding layers, giving rise to a fingerprint texture [(b) and (c)]. The pairs of lines and the director deformation near them are shown in detail in (d). Yellow lines represent $\lambda^{1/2}$ lines, while green lines show $\lambda^{-1/2}$ lines.

combined with the pairs of lines, and Fig. 2(c), which shows a developing $\lambda^{1/2}$ (yellow) and the nx component (red) of the director. Figure 2(d) shows a three-dimensional (3D) perspective of a p pair and three different director distributions perpendicular to the lines.

By combining the nz^2 component and the $\lambda^{1/2}$ lines, we see that the lines connect the individual fingers into a large mesh, shown in Fig. 3(a), where each end of a $\lambda^{1/2}$ line connects the extremes of a given finger [zoomed area of Fig. 3(a)]. Thus each line groups a pair of stripes, as described in Ref. [14].

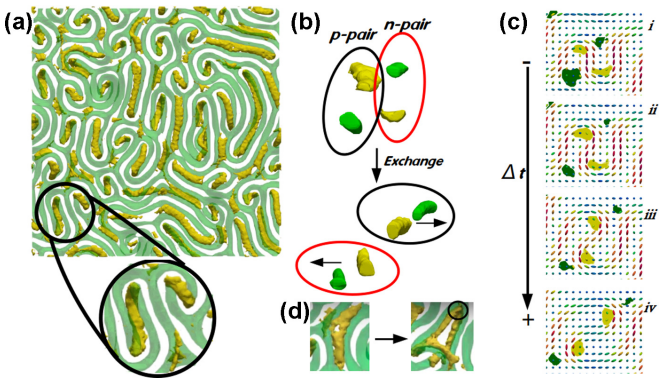

FIG. 3. Role of λ lines (a) in the fingerprint structure (here only $\lambda^{1/2}$ is shown), where the coreless lines connect different stripes. (b) and (c) show the interaction of two pairs of lines: Two pairs exchange pairs of lines (b), which adds a 2π turn to the sample. (c) shows this process as time evolves [(i)–(iv)], while (d) shows a top-view image of the process.

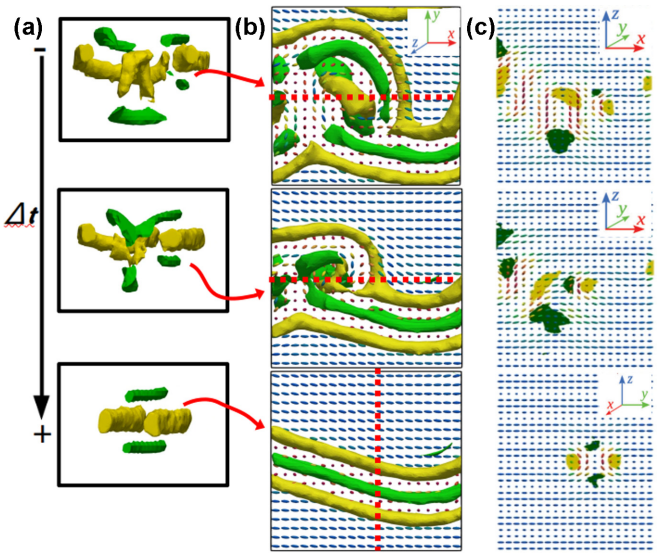

FIG. 4. Isosurface representation of the $\lambda^{-1/2}$ (in green) and $\lambda^{1/2}$ (in yellow) lines in the formation of a Lehmann cluster. (a) shows three pairs of lines interacting, resulting in a Lehmann cluster. (b) shows top-view images, while (c) shows side-view images with the directors. For (a)–(c), the top, middle, and bottom panels represent time evolution.

Hence the initial lines connecting fingers usually form a U-shaped structure, as seen in Fig. 2(d). However, this pair of nonsingular lines [Fig. 2(d)] is not compatible with the boundary conditions, so it is not stable. In this case, we observe an exchange of lines between p and n pairs at different slip planes. As shown in Fig. 3(b), the two dislocations of opposite configurations form a new kind of dislocation [Figs. 3(c-i)–3(c-iv)]; they appear to repel each other, thus promoting the inclusion of new twisted zones in the z direction. The structure shown in Fig. 3(c) resembles a CF1-type finger [33], adding 2π twist zones that, since homeotropic domains do not bind them as in typical CF1 fingers, expand, forming the Grandjean texture. This process appears to occur only in regions where the two pairs nearly overlap; so two $+1/2$ lines at different heights connect and initiate the nucleation of the Grandjean zone, as shown in Fig. 3(d). It is also important to notice how different the dynamics are if the CLC sample is not bounded (see free-boundary case below). In the SM, we also provide the polar angle and the pitch across the sample for three different times to better understand how the dynamics take place (see SM, Fig. S4).

The general behavior of the pairs of lines is to combine and form clusters with quadrupolar order, with $b = 0$, called Lehmann domains, often referred to as "oily streaks." Such clusters are much more stable than single pairs of defects since all the pairs eventually combine to form Lehmann domains.

Two kinds of dynamics lead to the formation of the Lehmann domains. First, two zones where Grandjean texture is developing may envelop a region where a dislocation (n pair or p pair) exists. In this case, as shown in Fig. 4, we see a p pair that is surrounded by two developing Grandjean zones. In this case, the two $-1/2$ lines from the pairs separating Grandjean zones combine, while the $+1/2$ (p pair), U-shaped defect gets annealed. The remaining $-1/2$ line from the p pair becomes part of the newly formed Lehmann cluster. This dynamic process is shown in Fig. 4(a) (3D view), Fig. 4(b) (view from above), and Fig. 4(c) (side view). The second commonly observed case occurs when two developing Grandjean zones meet, merging lines of the same kind and thus forming clusters directly. Once the clusters are formed, they separate Grandjean zones. A typical oily streak structure is shown in the bottom row of Fig. 4. However, during the relaxation dynamics, it is not uncommon to form defects with different core structures (larger width). However, these structures demand higher elastic energy and quickly disappear; so they either become the same defect as in Fig. 4 (see also videos in the SM) or form loops that shrink down [34].

During the relaxation process, several closed loops of finger structures, formed by Lehmann clusters, appear and eventually shrink, leaving behind the Grandjean texture. Figures 5(a)–5(e) show the coarsening dynamics of the nonsingular lines forming the cluster. The process occurs in nearly 80 ms. We first notice from the texture in Fig. 5(f) (region shown by the dashed rectangle) that the loop is in contact with another straight cluster. Indeed, the same $-1/2$ defect surrounds a $+1/2$ line at the center of the loop and acts as the upper $-1/2$ line of the linear cluster. As the loop shrinks, the $-1/2$ line is gradually replaced by $-1/2$ lines already existing in the straight cluster [shown in the zoomed area of Fig. 5(d) in blue]. In Fig. 5(g) we show how the loop area changes with $t_0 - t$, where t_0 is the time when the loop disappears. Initially, the loop decreases at $(t_0 - t)^{0.79}$, and later it changes at $(t_0 - t)^{1.2}$. The exponent is a function of the loop radius, as it presents two different values. The initial, slower behavior may be related to the initial replacement of the $-1/2$ line between the loop and the straight cluster. After this $-1/2$ line is replaced in the linear cluster, the annealing becomes faster, with exponent 1.2. Both exponents differ from those reported for the annealing of core defects [35,36] but present a similar value to measured exponents in twisted loop defects of bent-core materials [34]. Figure 5(h) shows a plane perpendicular to Fig. 5(a) (dashed red line), indicating that two clusters form the loop at different heights that anneal each other and form a modified structure cluster.

To better understand the effect of the strong anchoring on the homeotropic-to-planar transition, we now briefly discuss the dynamics of the same sample studied before. Still, now we consider an anchoring energy equal to zero, so there is no boundary effect during the transition. As in the strong-anchoring case, we assume periodic boundary conditions in the x and y directions and start by applying a strong electric field in the z direction, so the helix is completely unwound.

Here, unlike the case with strong anchoring, a twist does not start from the boundaries after the field is removed, but as expected, it happens everywhere across the sample, as shown in Fig. 6(a). Although the transient planar structure is still seen for this sample, the pathway to the Grandjean structure is somewhat different. Since twist and polar angle change occurs everywhere, we observe the formation of varying twist domains within the sample, which homeotropically aligned directors often separate, as observed inside the

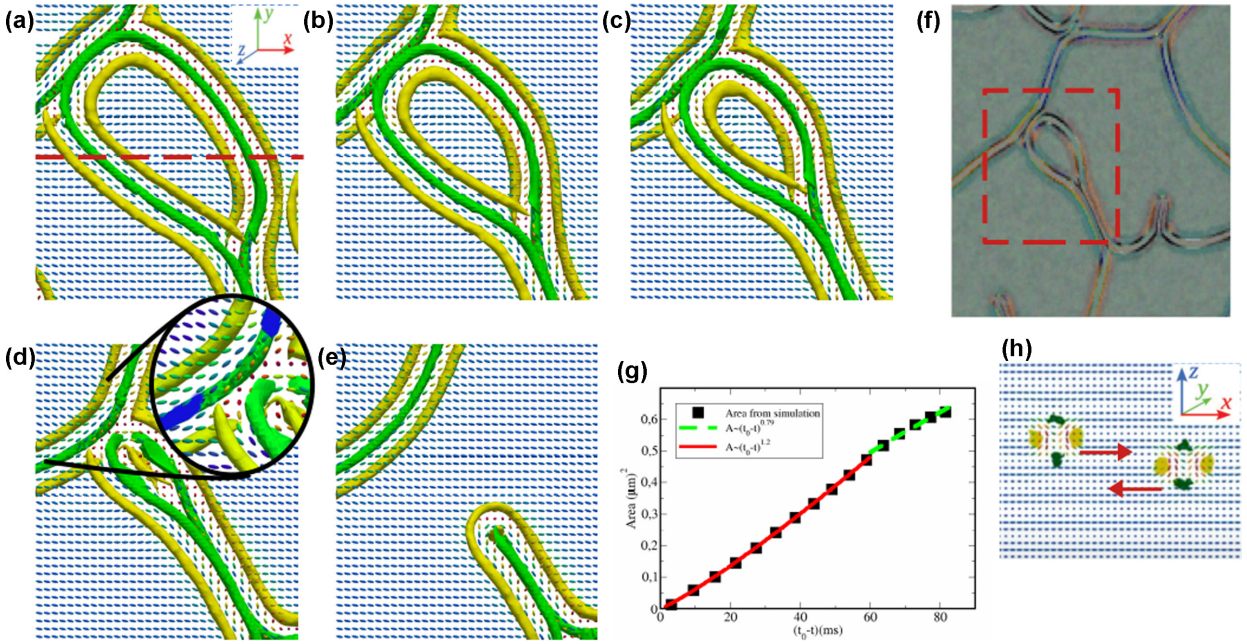

FIG. 5. Coarsening dynamics of Lehmann clusters. (a)–(e) show a shrinking loop formed by Lehmann clusters and how the different pairs of λ lines anneal during the process. (f) shows the calculated texture, displaying the characteristic oily streak pattern of CLCs. (g) shows the power-law nature of the shrinking process, formed by an initial slower process, with an exponent 0.79, followed by faster annealing, with an exponent 1.2. (h) shows the two clusters at different heights approaching each other to form a single cluster.

elliptical area in Fig. 6(b). From the texture point of view, the dark homeotropic texture begins to display small bright regions that quickly grow into a structure with several individual fingers that slowly relax to a more uniform texture as shown in Fig. 6(c) (arrows indicate time passage from the first to the last texture).

Then, as with strong anchoring, we notice some regions in which dislocations appear. However, here they result from

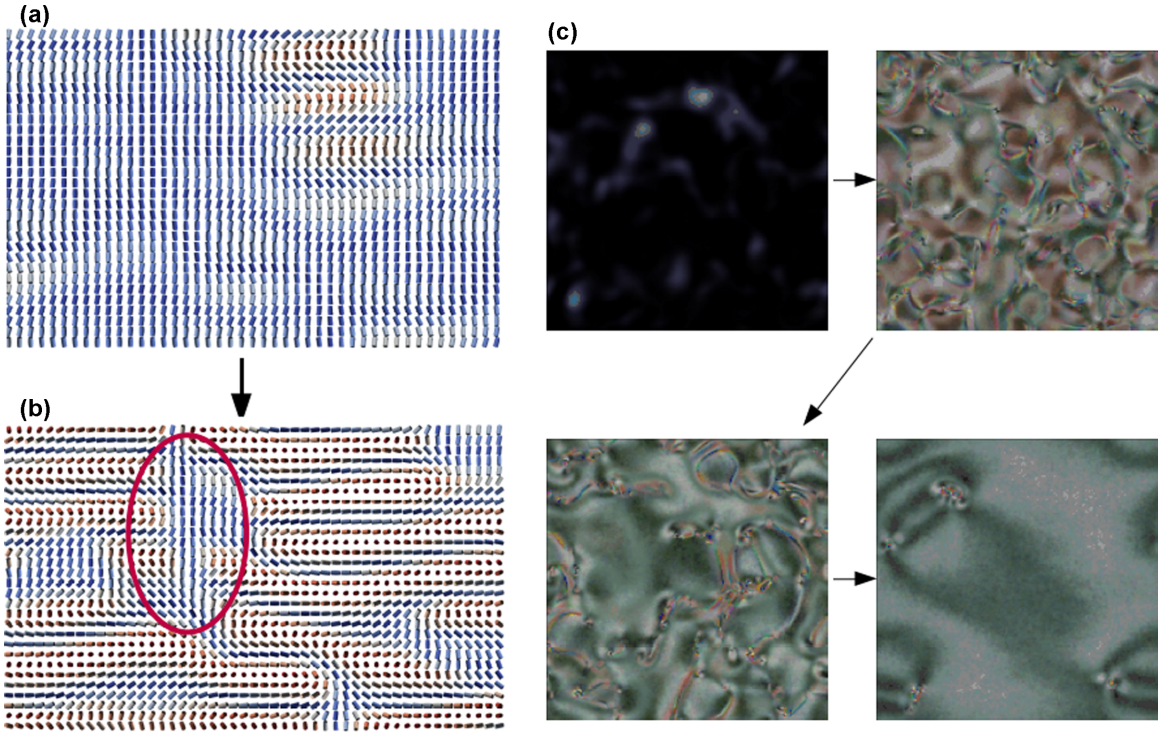

FIG. 6. Director field representation of the free-boundary case at the times (a) $t = 1.44$ ms and (b) $t = 1.97$ ms. (c) Textures at the respective times 1.37 ms, 2.13 ms, 13.54 ms, and 0.69 s.

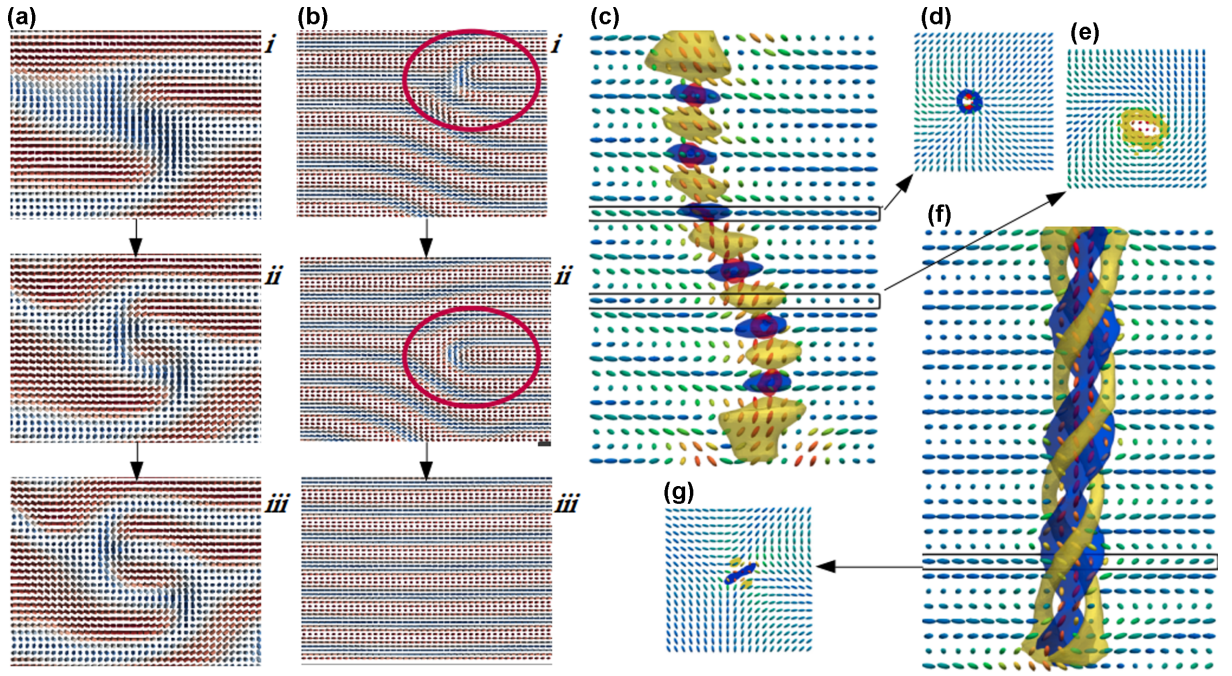

FIG. 7. Director field representation of (a) the mismatch of regions forming two pairs of $\lambda^{+1/2}\lambda^{-1/2}$ lines, at the times (i) 2.13 ms, (ii) 2.95 ms, and (iii) 3.82 ms, and (b) gliding of a pair $\lambda^{+1/2}\lambda^{-1/2}$ towards the bottom surface at the times (i) 33.44 ms, (ii) 0.11 s, and (iii) 3.49 s. The combination of the isosurface and director field representation for (c) a dissociated χ line, with the cross section of a (d) high-splay and (e) high-bend region, and (f) a spiral deformation and (g) its cross section.

the mismatch between areas with different numbers of turns, and they also add π turns by moving and interacting pairs of coreless lines. This is shown in Figs. 7(a-i)–7(a-iii). Another unique behavior of this sample compared with the strong-anchoring case is the glide of dislocations. Since there are no substrates to hinder dislocation glide, one can see dislocations moving up and down toward the free boundaries to decrease the elastic energy of the system, as shown in Figs. 7(b-i)–7(b-iii).

Another interesting structure in this sample is the formation of defects in the vicinity of two different domains. Two kinds of structures are observed: First, because of the out-of-register layers, one may expect the formation of χ lines [29]. Instead, we observe a dissociated structure, formed by rings of $\lambda^{1/2}$ and $\tau^{-1/2}$ lines, as shown in Fig. 7(c), where the yellow zones represent the lower values (high bend) and the blue regions represent the higher values (high splay) of the S_{SB} parameter. In contrast, the red isolines represent the core defect line. Figures 7(d) and 7(e) show the cross section of the core defect ring and the coreless defect ring, respectively. The second kind of structure we observed in this sample is composed of a double helix formed by two $\lambda^{1/2}$ defect lines, shown in Fig. 7(f). This structure does not present any core defect, which is more common across the sample. Figure 7(g) shows the cross section of this structure, where the yellow and blue isosurfaces represent the S_{SB} parameter as before. Both the structure shown in Fig. 7(c) and the structure shown in Fig. 7(f) are metastable and eventually shrink down, so that the neighbor domains connect. Furthermore, in some cases, the two structures get connected by a pair of λ lines, as shown in Figs. 8(a) and 8(b). In this case, instead of running across the whole sample, the domain boundaries reach a certain height, above which the CLC layers are in register. Figure 8(b) shows how more than one such structure may get connected. Figures 8(c-i)–8(c-iv) show how the two structures eventually merge, giving rise to perfectly aligned CLC layers.

Our simulations were allowed to run (from the time evolution point of view) from a few milliseconds to several seconds until the system reached an equilibrium point. We output the system's state in a logarithmic fashion, so a more significant number of states are obtained in the initial stages and fewer for longer times. For every state we output, we interpolate the mesh to get the directors and calculate Frank's total elastic energy and the individual energies of splay, twist, and bend.

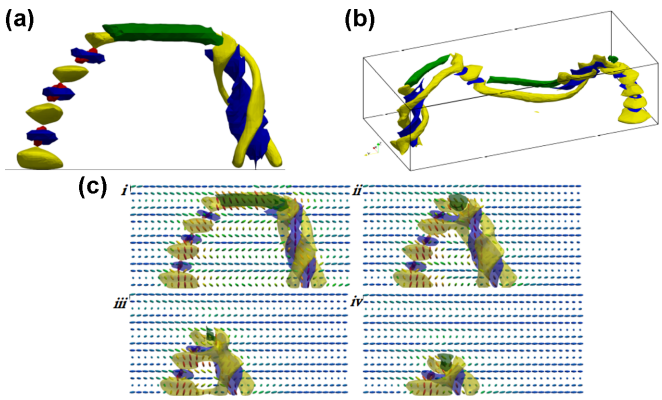

FIG. 8. Dynamics of the free sample: (a) Dissociated ξ line connected with a spiral deformation by a pair of λ lines. (b) Another region shows three structures connected by pairs of λ lines. (c) Merging and annealing of defect structures during the dynamical process [(i)–(iv)], leading to the aligned helical structure.

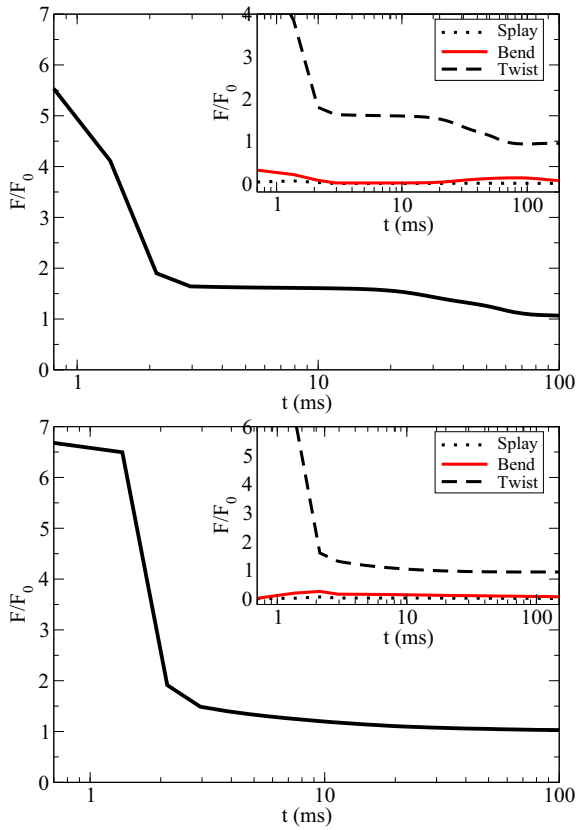

FIG. 9. Scaled total elastic energy F/F_0 vs $\log(t)$ for both samples studied in this paper. In the top panel, the strong-anchoring case is shown, while the bottom panel shows the free-boundary sample. The insets show the individual energies of splay, twist, and bend.

The top and bottom panels of Fig. 9 show the total elastic energy F divided by the final elastic energy F_0 for the sample with strong anchoring and the sample with free boundaries, respectively, versus $\log(t)$. The insets show the individual energies, also normalized by F_0. In both cases, the twist energy is the dominant contribution, while splay is nearly neglectable. Furthermore, it is interesting to notice how points of high bend energy occur when the twist energy decreases, which is best observed in the top panel of Fig. 9, representing the situation with strong anchoring. In this case, while initially the bend energy is high during the formation of the transient planar structure, it also increases around 70 ms, representing the bend of cholesteric layers, leading to the formation of the λ line defects.

In conclusion, we investigated the dynamics of a CLC winding up from an unwound state in a slab cell. This simulation procedure is capable of describing all the relaxation states, from the unwound condition to the Grandjean texture. Our results indicate that the twist starts from the substrates, first forming the transient planar texture, and then slowly passing through deformed states. Among them, the system forms wrinkled states, which in turn leads to dislocations in high-bend regions, characterized in terms of pairs of coreless lines. Core defects are not observed through the whole dynamics. The pairs of coreless lines displace layers around them and are the ending points of the fingerprint texture that forms next. As time passes, a rich scenario involving interaction and exchange of pairs creates quadrupolar structures (Lehmann clusters). The clusters are metastable structures but are commonly observed in experimental samples. Our simulations have provided some indications of how Lehmann clusters interact and anneal. A direct comparison of these simulations with experimental measurements of oily streak coarsening, which appears never to have been explored in the literature [37], would be a clear next step.

ACKNOWLEDGMENTS

The authors thank CNPq and CAPES for their financial support. This work was partially supported by the National Institute of Science and Technology of Complex Fluids (INCT-CFx). R.S.Z. thanks CNPq for support under Process No. 304634/2020-4. R.F. de Souza thanks Financiadora de Estudos e Projetos (FINEP) for support under Process No. 0113032700. This research was developed with the support of LAMAP-UTFPR.

[1] Z. Chen, G. Huang, I. Trase, X. Han, and Y. Mei, Phys. Rev. Appl. **5**, 017001 (2016).
[2] H. Zhao, K. Li, M. Han, F. Zhu, A. Vázquez-Guardado, P. Guo, Z. Xie, Y. Park, L. Chen, X. Wang, H. Luan, Y. Yang, H. Wang, C. Liang, Y. Xue, R. D. Schaller, D. Chanda, Y. Huang, Y. Zhang, and J. A. Rogers, Proc. Natl. Acad. Sci. USA **116**, 13239 (2019).
[3] O.-Y. Zhong-can and L. Ji-xing, Phys. Rev. Lett. **65**, 1679 (1990).
[4] M. H. Godinho, J. P. Canejo, G. Feio, and E. M. Terentjev, Soft Matter **6**, 5965 (2010).
[5] Y. Sawa, F. Ye, K. Urayama, T. Takigawa, V. Gimenez-Pinto, R. L. B. Selinger, and J. V. Selinger, Proc. Natl. Acad. Sci. USA **108**, 6364 (2011).
[6] L. T. de Haan, J. M. N. Verjans, D. J. Broer, C. W. M. Bastiaansen, and A. P. H. J. Schenning, J. Am. Chem. Soc. **136**, 10585 (2014).
[7] A. Agrawal, T. Yun, S. L. Pesek, W. G. Chapman, and R. Verduzco, Soft Matter **10**, 1411 (2014).
[8] S. Iamsaard, S. J. Aßhoff, B. Matt, T. Kudernac, J. J. L. M. Cornelissen, S. P. Fletcher, and N. Katsonis, Nat. Chem. **6**, 229 (2014).
[9] A. Jákli, O. D. Lavrentovich, and J. V. Selinger, Rev. Mod. Phys. **90**, 045004 (2018).
[10] R. L. Biagio, R. T. Souza, L. R. Evangelista, and R. S. Zola, J. Mater. Chem. C **9**, 8623 (2021).
[11] S. Wu and D. Yang, *Fundamentals of Liquid Crystal Devices*, Wiley Series in Display Technology (Wiley, New York, 2006).
[12] D. Yang, J. L. West, L. Chien, and J. W. Doane, J. Appl. Phys. **76**, 1331 (1994).
[13] P. Watson, V. Sergan, J. E. Anderson, J. Ruth, and P. J. Bos, Liq. Cryst. **26**, 731 (1999).
[14] P. Watson, J. E. Anderson, V. Sergan, and P. J. Bos, Liq. Cryst. **26**, 1307 (1999).

[15] P. Watson, J. E. Anderson, V. Sergan, and P. J. Bos, Liq. Cryst. **28**, 1 (2001).
[16] V. Sergan, Y. Reznikov, J. Anderson, P. Watson, J. Ruth, and P. Bos, Mol. Cryst. Liq. Cryst. Sci. Technol. Sect. A **330**, 95 (1999).
[17] M.-H. Lee, Y.-C. Yang, J.-E. Kim, and H. Y. Park, Phys. Rev. E **68**, 051701 (2003).
[18] M.-H. Lee, J.-E. Kim, and H. Y. Park, Liq. Cryst. **31**, 333 (2004).
[19] I.-A. Yao, J.-J. Wu, and S.-H. Chen, Jpn. J. Appl. Phys. **43**, 1488 (2004).
[20] I.-A. Yao, J.-J. Wu, and S.-H. Chen, Jpn. J. Appl. Phys. **43**, 705 (2004).
[21] D.-K. Yang and Z.-J. Lu, Dig. Tech. Pap. - Soc. Inf. Disp. Int. Symp. **26**, 351 (1995).
[22] Y.-C. Yang, R. S. Zola, Y. Cui, D.-K. Yang, H.-Y. Chen, C.-C. Hsu, C.-J. Chen, and C.-C. Liang, Dig. Tech. Pap. - Soc. Inf. Disp. Int. Symp. **42**, 400 (2011).
[23] M. Yu, X. Zhou, J. Jiang, H. Yang, and D.-K. Yang, Soft Matter **12**, 4483 (2016).
[24] S. Čopar, T. Porenta, and S. Žumer, Liq. Cryst. **40**, 1759 (2013).
[25] See Supplemental Material at http://link.aps.org/supplemental/10.1103/PhysRevE.106.064701 for supplemental equations, figures, and videos.
[26] R. de Souza, E. Omori, and R. Zola, Comput. Phys. Commun. **277**, 108379 (2022).
[27] H. Mori, E. C. Gartland, J. R. Kelly, and P. J. Bos, Jpn. J. Appl. Phys. **38**, 135 (1999).
[28] T. Machon and G. P. Alexander, Phys. Rev. X **6**, 011033 (2016).
[29] P. de Gennes and J. Prost, *The Physics of Liquid Crystals*, International Series of Monographs on Physics (Clarendon, Oxford, 1993).
[30] C. A. Whitfield, T. C. Adhyapak, A. Tiribocchi, G. P. Alexander, D. Marenduzzo, and S. Ramaswamy, Eur. Phys. J. E **40**, 50 (2017).
[31] I. I. Smalyukh and O. D. Lavrentovich, Phys. Rev. E **66**, 051703 (2002).
[32] B. I. Senyuk, I. I. Smalyukh, and O. D. Lavrentovich, Phys. Rev. E **74**, 011712 (2006).
[33] I. I. Smalyukh, B. I. Senyuk, P. Palffy-Muhoray, O. D. Lavrentovich, H. Huang, E. C. Gartland, V. H. Bodnar, T. Kosa, and B. Taheri, Phys. Rev. E **72**, 061707 (2005).
[34] K. S. Krishnamurthy, P. Tadapatri, and W. Weissflog, Soft Matter **7**, 6273 (2011).
[35] Z. Tan and G. C. Berry, J. Rheol. **47**, 73 (2003).
[36] I. Chuang, N. Turok, and B. Yurke, Phys. Rev. Lett. **66**, 2472 (1991).
[37] M. Zapotocky, L. Ramos, P. Poulin, T. C. Lubensky, and D. A. Weitz, Science **283**, 209 (1999).